Formation kinetics of the Mo(100)-Ag $c(2\times2)$ surface alloy

K. L. Man, Y. J. Feng, and M. S. Altman*

Department of Physics, Hong Kong University of Science and Technology, Clear Water Bay, Kowloon, Hong Kong
(Received 3 March 2006; revised manuscript received 27 June 2006; published 30 August 2006)

Kinetic processes that affect the formation and ordering of the Ag-induced $c(2\times2)$ alloy at the Mo(100) surface have been investigated with low-energy electron microscopy and diffraction. A kinetic limitation to alloy formation, which is believed to be associated with the exchange of Ag for Mo surface atoms, is observed during Ag deposition below about 750 K. The controlling activation barrier is determined to be $E_{ex}=0.50\pm0.17$ eV. These investigations also reveal that disorder is built into the alloy during the formation process to a degree that is determined by nucleation kinetics, which are governed by diffusion, and a diffusion barrier of $E_{dif}=0.25\pm0.03$ eV is determined. This low diffusion barrier is attributed to the formation and motion of an intermediate Ag-Mo-vacancy complex prior to exchange. Evidence of desorption is also observed above 950 K with a characteristic desorption energy of $E_{des}=2.81\pm0.34$ eV.

I. INTRODUCTION

Atoms that are deposited on a surface of a dissimilar material may either remain on the surface as an overlayer or they may become incorporated in a surface or bulk alloy. Surface alloy formation is recognized to be a fairly common phenomenon because of its occurrence in numerous adsorbate-substrate systems.[1–26] Practical interest in the chemical properties of surface alloys has led to the identification of novel chemisorption and catalytic behavior. Many previous investigations of surface alloys have focused on detailed geometric and electronic structure determination. Theoretical investigations aimed at verifying or predicting surface alloy structures have also provided key insight on the origins of surface alloy formation in diverse systems. Although the energetics that govern the stability of overlayer vs surface alloy structures can be understood in many systems, the kinetics of alloy formation and ordering is less well understood.

We have investigated the formation of the Ag-induced $c(2\times2)$ alloy at the Mo(100) surface. Several metals are known to induce related $c(2\times2)$ alloys at the Mo(100) and W(100) surfaces, including Cu, Ag, Au/W(100),[22–24] Pd/Mo(100)[25] and Cu, Ag, and Au/Mo(100).[26] In the $c(2\times2)$ alloy structure, metal atoms substitute for surface Mo or W atoms in a checkerboard pattern (Fig. 1), with an ideal metal coverage of 0.5 monolayer (ML). Cu and Ag-induced $c(2\times2)$ structures were also observed on Mo(100) previously[27,28] but were interpreted erroneously in terms of overlayer arrangements.[28] In our recent investigations, first principles total energy calculations showed that Cu, Ag, and Au-induced $c(2\times2)$ alloys on the Mo(100) surface are energetically favorable compared to $c(2\times2)$ and (1×1) overlayer arrangements at 0.5 ML coverage.[26] Alloy formation in these systems was also confirmed by low-energy electron microscopy (LEEM) and diffraction (LEED) measurements.[26]

Local density approximation calculations showed previously that the Mo(100) and W(100) surfaces are very nearly unstable with respect to the formation of a $c(2\times2)$ vacancy array.[29,30] They also demonstrated that electron depletion induced by an applied electric field can tip the balance strongly

in favor of the $c(2\times2)$ vacancy array.[30] This result could explain why a $c(2\times2)$ vacancy array was produced earlier in field desorption experiments on the W(100) surface in Ref. 31. Another thing that the calculations revealed is that there is no significant bond formation between metal adsorbate and substrate atoms in the alloy structure, which was interpreted to mean that the alloy is not stabilized by d-bonding.[29] It also prompted the speculation that charge depletion, similar to that which is induced by an applied field, is responsible for stabilizing a vacancy array in which metal adsorbate atoms take up residence in the alloy structure.[30] Recent calculations confirmed that charge transfer does indeed occur from the substrate to the metal adsorbate atoms in the $c(2\times2)$ alloy structure without obvious chemical bond formation.[32] Occupied surface states at the X point were also identified, which are shifted to larger binding energy in the alloy structure as compared to corresponding states in the vacancy array on Mo(100) and W(100).[32] This should also clearly contribute to the stability of the alloy structures on these
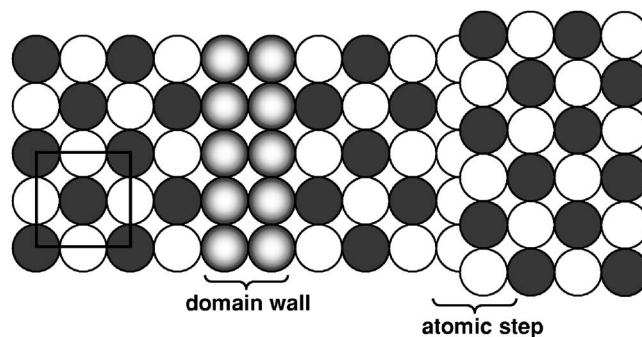

FIG. 1. Model of the $c(2\times2)$ alloy structure in which Ag atoms (shaded circles) replace Mo atoms (open circles) in the surface in a checkerboard arrangement. The unit cell is indicated. Two possible $c(2\times2)$ sublattices exist on the Mo(100) surface, which are laterally shifted by one lattice vector. Coalescence of alloy domains on different sublattices produces a domain wall. The locations of Ag and Mo atoms in the domain wall (shaded circles) are not specified. The shifted registry of adjacent terraces separated by an atomic step is also shown.

surfaces. Other factors that have not yet been identified may also contribute to the alloy stability.

In the present work, we first extend previous first principles calculations to consider the energetics of overgrowth of the Ag-induced $c(2 \times 2)$ alloy on Mo(100) by a Ag layer. The more complete view of the energy landscape (at $T=0$) that this provides is generally a useful input for understanding and modeling experimental data that identify kinetic effects in the alloy formation. For example, well-ordered $c(2 \times 2)$ alloy structures on Mo(100) and W(100) were previously observed only upon annealing a metal covered surface or during metal deposition at elevated temperature, typically higher than 700 K.[22–26] We study the kinetic limitation to alloy formation at low temperature carefully here and determine the corresponding activation barrier, which is believed to be associated with the exchange of Ag for surface Mo atoms. In addition, the formation and ordering of the $c(2 \times 2)$ alloy are evidently influenced by nucleation kinetics, which are governed by diffusion. A diffusion activation barrier is determined that is too low to be realistically ascribed to a hopping diffusion mechanism and is also lower than the exchange barrier. Recognizing that the Mo(100) surface is prone to vacancy formation, we suggest that diffusion is mediated by the formation and motion of an intermediate Ag-Mo-vacancy complex prior to exchange. Evidence of desorption is also observed at higher temperature, which prevents condensation of sufficient material to attain the ideal $c(2 \times 2)$ coverage of 0.5 ML, and the activation energy for desorption is determined.

II. THEORETICAL METHOD AND RESULTS

The total energy calculations were carried out with the local-density-functional formalism, employing ultrasoft pseudopotentials with the generalized gradient approximation (PW91) form of exchange-correlation functionals and a plane wave basis with cutoff kinetic energy of 300.0 eV.[33,34] We use the standard repeated slab geometry, which consists of 11 atomic layers and a vacuum of 11 Å. All atomic positions were relaxed until the total energy converged to the order of 0.1 meV. A 12×12 uniform grid in the two-dimensional Brillouin zone was used for k-point sampling.[35]

The calculated heats of formation per Ag atom for (A) the $c(2 \times 2)$ surface alloy at 0.5 ML coverage, (B) the $c(2 \times 2)$ overlayer at 0.5 ML, (C) the (1×1) overlayer at 1.0 ML, and (D) the $c(2 \times 2)$ alloy covered by a Ag monolayer at 1.5 ML are shown in Fig. 2 relative to (O) the clean surface. We denote the Ag-covered $c(2 \times 2)$ alloy at 1.5 ML coverage as $c(2 \times 2)_{1.5}$ to distinguish it from the $c(2 \times 2)$ alloy at 0.5 ML coverage. Two other possible configurations at 0.5 ML coverage are (E) a surface that is half covered by (1×1) overlayer and uncovered on the remaining half and (F) a surface that is one-third covered by a $c(2 \times 2)_{1.5}$ alloy and uncovered on the remaining two-thirds. The heats of formation for these configurations are indicated by the open symbols at 0.5 ML on the lines that interpolate between the points OC and OD, respectively, in Fig. 2. Another possible configuration at 1.0 ML coverage is (G) a surface that is covered by $c(2 \times 2)$
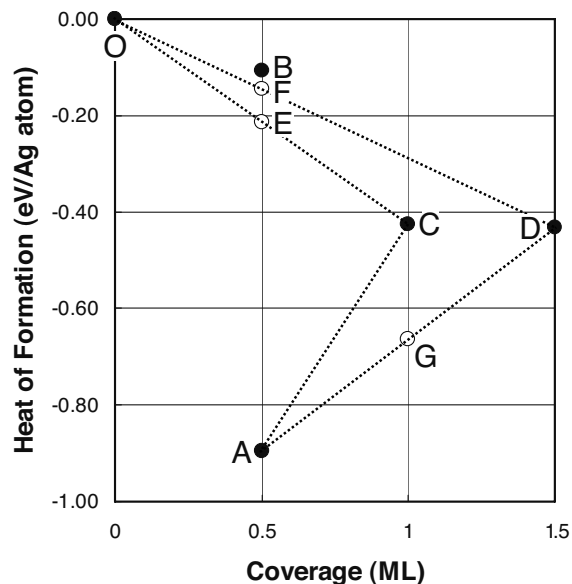

FIG. 2. The heat of formation per Ag atom relative to the clean surface (O) for the (A) $c(2 \times 2)$ alloy, (B) $c(2 \times 2)$ overlayer, (C) (1×1) overlayer, and (D) $c(2 \times 2)$ alloy covered by a Ag monolayer. Points E, F, and G correspond to mixtures of OC, OD, and AD, respectively.

alloy on one half and by the $c(2 \times 2)_{1.5}$ alloy on the other half. The heat of formation for this configuration is indicated by the open symbol at 1.0 ML on the line AD in Fig. 2.

The heat of formation for the $c(2 \times 2)$ alloy is substantially more negative than the three other structures at 0.5 ML coverage. This indicates that the $c(2 \times 2)$ alloy is the energetically favored configuration at $T=0$. The (1×1) overlayer and $c(2 \times 2)_{1.5}$ alloy are both metastable at 0.5 ML and below, although the (1×1) is the energetically favored of the two (compare lines OC and OD in Fig. 2). On the other hand, the calculation results also indicate that overgrowth of the $c(2 \times 2)$ alloy by a Ag layer above 0.5 ML is energetically favorable compared to the conversion of the $c(2 \times 2)$ alloy to a (1×1) overlayer at $T=0$ (compare line AD to line AC, respectively, in Fig. 2). The heats of formation for configurations in which metal atoms are substituted for Mo in deeper layers were found to be large and positive. This is not surprising since face-centered-cubic (fcc) metals generally do not dissolve in refractory metals, which have much higher cohesive energy.[36]

III. EXPERIMENTAL RESULTS AND ANALYSIS

A. Experimental details

The LEED measurements described here were performed in a low-energy electron microscope. The imaging and diffraction principles in LEEM have been described previously.[37] The Mo sample was oriented to within 0.1° of the [100] direction. It was cleaned by annealing at 1200 K in an oxygen pressure of 1×10^{-7} Torr and flashing to 2000 K. The sample temperature was measured by a W/Re 3%$-W/Re$25% thermocouple that was attached to the
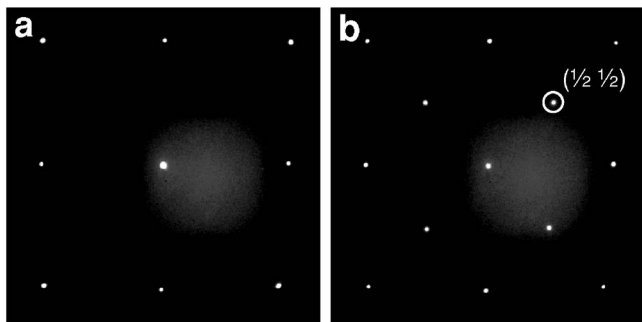
FIG. 3. LEED patterns of (a) the clean Mo(100) (1×1) surface, and (b) the Ag-induced $c(2\times2)$ surface alloy at incident electron energy $E=32$ eV. The $(\frac{1}{2}\ \frac{1}{2})$ spot of the $c(2\times2)$ pattern is indicated.

sample holder immediately adjacent to the side of the sample. The accuracy of the temperature measurement was improved by calibrating the thermocouple at 1400 K with a disappearing filament optical pyrometer using an emissivity setting of 0.17.[38] The growth experiments were performed by depositing Ag on the surface at various fixed temperatures and deposition rates. Ag was deposited reproducibly from an electron-beam-heated crucible in a deposition source that was equipped with water cooling and internal flux monitor by proportional ion current measurement. The pressure rose from the base pressure of 5×10^{-11} Torr to the low 10^{-10} Torr range during Ag deposition. The deposition rate was calibrated by recording the deposition time required for the $c(2\times2)$ diffraction integrated intensity to reach a maximum at a temperature, $T=800$ K, where the alloy forms without kinetic limitation (see Sec. III C). The deposition rate is then calculated as the ideal Ag coverage in the alloy, 0.5 ML, divided by the required deposition time. The deposition rate that was determined in this way was found to scale linearly with the ion current that was detected by the internal flux monitor of the deposition source, which is the expected behavior. This calibration was performed periodically during the full duration of the investigations.

B. Structure and morphology

The clean surface exhibited a sharp, intense (1×1) diffraction pattern [Fig. 3(a)], and LEEM images showed large, flat terraces separated by monoatomic steps [Fig. 4(a)]. The deposition of Ag on the Mo(100) surface produced a sharp, intense $c(2\times2)$ diffraction pattern [Fig. 3(b)] if the deposition temperature was sufficiently high, typically above 700 K. LEEM also revealed the nucleation and growth of many small compact islands during the initial formation of the surface alloy [Fig. 4(b)]. This dramatic change of the surface morphology occurs when Ag exchanges for surface Mo atoms, which then combine with Ag adatoms to form alloy islands. With increasing Ag coverage, alloy islands nucleate on increasingly shorter length scales [Fig. 4(c)] until the surface has a very rough appearance by the time the Ag coverage reaches the ideal coverage of 0.5 ML [Fig. 4(d)]. Thus, the alloy formation effectively converts an initially flat surface to a two-level alloy surface with alloy islands surrounded by alloyed terrace [Fig. 4(e)]. At lower deposition
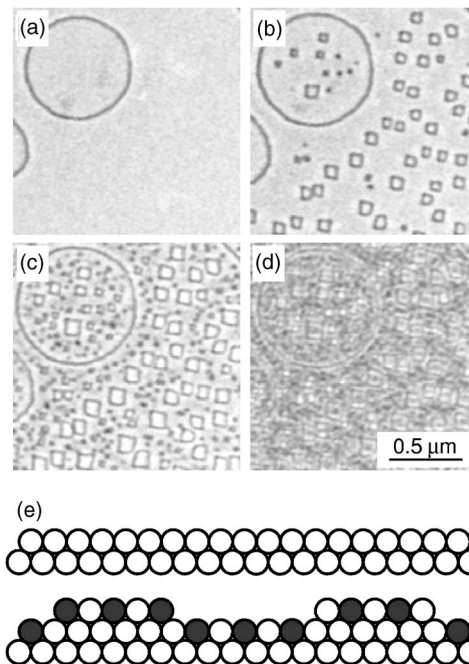

FIG. 4. LEEM images of surface morphological changes that are caused by alloy formation during Ag deposition on Mo(100) at $T=900$ K: (a) clean surface, (b) Ag coverage $\theta=0.16$ ML, (c) $\theta=0.33$ ML, and (d) $\theta=0.50$ ML. The dark lines are monoatomic steps. The imaging energy was 6.0 eV. The initial flat surface and the ideal two-level surface alloy are shown schematically in (e). The filled and open circles in (e) are Ag and Mo atoms, respectively.

temperatures, formation of the $c(2\times2)$ alloy was kinetically limited. Information about this kinetic limitation and other kinetic processes that affect the formation of the Ag-induced $c(2\times2)$ alloy on Mo(100) was obtained by monitoring the integrated diffraction intensity in the $(\frac{1}{2}\ \frac{1}{2})$ spots of the $c(2\times2)$ diffraction pattern.

C. Exchange

The integrated $c(2\times2)$ diffraction intensity increased initially during Ag deposition until it reached a well-defined maximum [Fig. 5(a)]. The maximum intensity occurred at a coverage, $\theta_{I\,max}$, that is shown in Fig. 5(b) vs deposition temperature. Exceeding this coverage caused the $c(2\times2)$ intensity to decrease [Fig. 5(a)]. Within experimental uncertainty, $\theta_{I\,max}$ was independent of the deposition rate. The data in Fig. 5(b) are averaged for deposition rates of 0.14, 0.21, 0.29, 0.39, and 0.43 ML/min, and the error bars represent the scatter for the different rates. The maximum $c(2\times2)$ intensity ideally occurs at a coverage of $\theta_{I\,max}=0.5$ ML in the absence of kinetic limitations. According to Fig. 5(b), this is the case for deposition at 800 K and above. After reaching a peak at $\theta_{I\,max}=0.5$ ML in this high-temperature range, the $c(2\times2)$ intensity decreased nearly to zero at 1 ML Ag coverage during deposition [Fig. 5(a)]. This suggests that dealloying and the formation of a (1×1) overlayer occur when the coverage exceeds 0.5 ML during deposition at 800 K and above. This experimental result is surprising because it
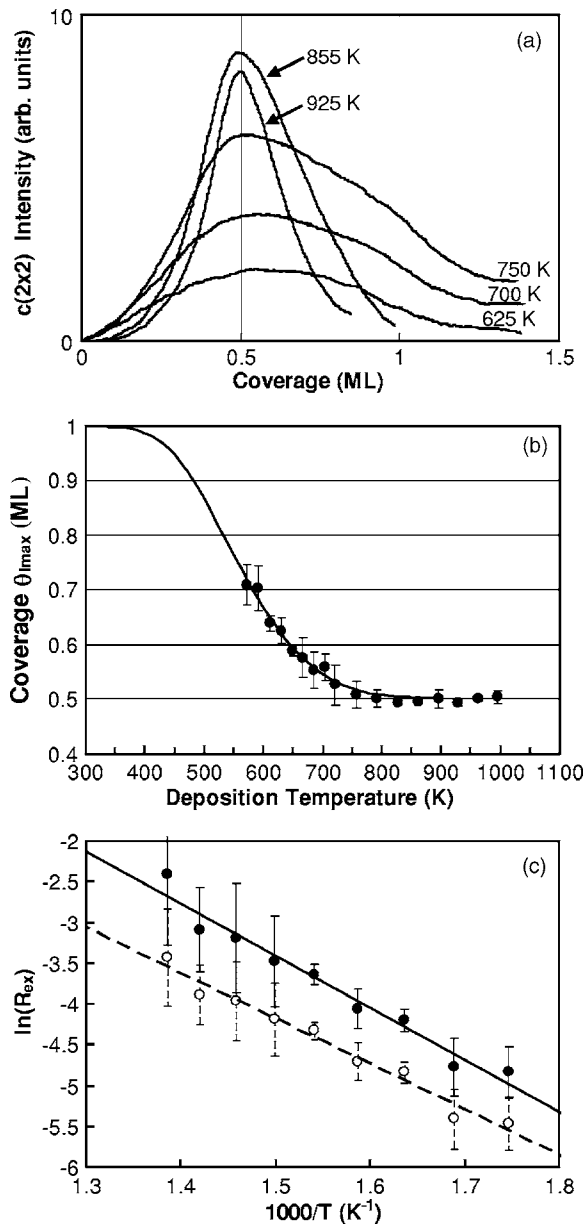
FIG. 6. The sharp decrease of the integrated intensity in the $\left(\frac{1}{2}\,\frac{1}{2}\right)$ LEED spots of the Mo(100)-Ag $c(2\times2)$ surface alloy above 800 K identifies an order-disorder transition (from Ref. 26). The intensities have been normalized to the average intensity below 800 K after correction for thermal diffuse scattering. The incident electron energy was 25.0 eV.

800 K by a dealloying mechanism.[26] Disordering via dealloying converts the ordered alloy to a disordered overlayer. The decrease of the $c(2\times2)$ intensity that is caused by disordering above 800 K is reproduced from Ref. 26 in Fig. 6. In the transition region above 800 K, ordered $c(2\times2)$ alloy and disordered Ag overlayer coexist in proportions that change with temperature and produce the intensity variation in Fig. 6. The dealloying that is apparently indicated here when θ exceeds 0.5 ML during deposition above 800 K may be related to the thermal instability of the ideal alloy at $\theta=0.5$ ML but is not fully understood. However, the incomplete understanding of dealloying above 800 K should not detract from the present discussion of alloy formation kinetics, which is based on measurements that were performed at lower temperature.

In contrast to the behavior above 800 K, a delay of the maximum $c(2\times2)$ intensity, $\theta_{\text{I max}} > 0.5$ ML, was observed during deposition at lower temperature [Fig. 5(b)]. The decrease of the $c(2\times2)$ intensity after its peak at $\theta_{\text{I max}}$ during deposition below 800 K also differed qualitatively from the behavior above 800 K. In particular, the $c(2\times2)$ intensity decreased to a nonzero minimum at a coverage that clearly exceeded 1 ML during deposition below 800 K [Fig. 5(a)]. We consider two scenarios that invoke formation of the metastable (1×1) overlayer and $c(2\times2)_{1.5}$ alloy structures to explain these two observations. A basic assumption in both cases is that the $c(2\times2)_{1.5}$ alloy produces a weaker $\left(\frac{1}{2}\,\frac{1}{2}\right)$ diffraction intensity than the $c(2\times2)$ alloy at the energy $E=25$ eV that the measurements were performed.

In the first scenario, the intensity behavior of present interest are attributed solely to the formation of the $c(2\times2)_{1.5}$ structure. The delay of $\theta_{\text{I max}}$ during deposition below 800 K, in particular, could occur if a Ag layer begins to grow on the $c(2\times2)$ alloy before the latter completely covers the surface. The peak $c(2\times2)$ diffraction intensity would then occur when the resulting mixture of $c(2\times2)$ and $c(2\times2)_{1.5}$ alloys covers the surface. This condition is expressed as the constraint on the area fractions, A, of the two alloy structures, $1 = A_{c(2\times2)} + A_{c(2\times2)1.5} = 2\theta_{c(2\times2)} + (2/3)\theta_{c(2\times2)1.5}$, where

FIG. 5. (a) Integrated $c(2\times2)$ diffraction intensity at the $\left(\frac{1}{2}\,\frac{1}{2}\right)$ positions vs time during Ag deposition on the Mo(100) surface at various indicated temperatures for a deposition rate of 0.21 ML/min. (b) The Ag coverage, $\theta_{\text{I max}}$, corresponding to the maximum $c(2\times2)$ integrated intensity during deposition is plotted vs deposition temperature. The solid line is the prediction of the rate equations model [Eq. (1)] for the parameters described in the text. (c) The logarithm of the exchange rate, R_{ex}, determined by the rate equations model is plotted vs inverse temperature for the limiting cases, (●) $\alpha=0$ and (○) $\alpha=1$, that are described in the text.

clearly contradicts the results of first principles calculations, which indicate that an equal mixture of $c(2\times2)$ and $c(2\times2)_{1.5}$ structures (point G in Fig. 2) is energetically favorable compared to a (1×1) overlayer at 1 ML coverage (point C in Fig. 2). The system should likewise follow a trajectory along line AD in Fig. 2 (in equilibrium at $T=0$), rather than along line AC. However, it should be noted that the ideal $c(2\times2)$ alloy surface at 0.5 ML coverage disorders above
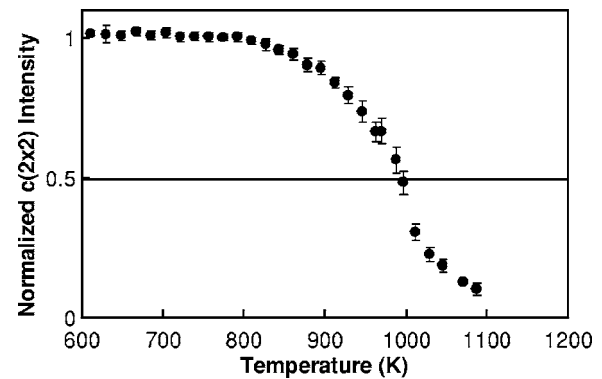
$\theta_{c(2\times2)}$ and $\theta_{c(2\times2)1.5}$ are the quantities of Ag in the two alloy structures at $\theta_{I\,max}$. Then $\theta_{I\,max}$ is given by $\theta_{I\,max}=\theta_{c(2\times2)}+\theta_{c(2\times2)1.5}$. After the intensity peak at $\theta_{I\,max}$, the intensity would then decrease as the remaining exposed $c(2\times2)$ alloy is covered by Ag. According to this scenario, the minimum diffraction intensity would eventually be reached when the complete $c(2\times2)$ alloy layer is covered by a complete Ag layer at 1.5 ML, i.e., the ideal $c(2\times2)_{1.5}$ alloy coverage. However, this model prediction is contradicted by the experimental data, which indicate that the minimum intensity is reached at a Ag coverage that is somewhat less than 1.5 ML and decreases toward 1 ML as the deposition temperature is lowered. Another reason to question the merit of this scenario is that the $c(2\times2)_{1.5}$ alloy is metastable compared to the (1×1) overlayer at coverages below $\theta_{I\,max}$ (compare line OD to line OC in Fig. 2). Of the two structures, the (1×1) overlayer should form rather than the $c(2\times2)_{1.5}$ alloy while clean Mo(100) surface is still exposed at coverages less than $\theta_{I\,max}$.

The second scenario that is considered accordingly invokes the formation of the (1×1) overlayer in parallel with the $c(2\times2)$ alloy up to $\theta_{I\,max}$. In this scenario, overgrowth of the $c(2\times2)$ alloy by a Ag layer does not commence until the surface is already covered by a mixture of (1×1) overlayer and $c(2\times2)$ alloy at $\theta_{I\,max}$. This optimal condition is expressed as the constraint on the area fractions of the two structures, $1=A_{c(2\times2)}+A_{(1\times1)}=2\theta_{c(2\times2)}+\theta_{(1\times1)}$, where $\theta_{(1\times1)}$ is the quantity of Ag in the overlayer at $\theta_{I\,max}$. Then $\theta_{I\,max}$ is given by $\theta_{I\,max}=\theta_{c(2\times2)}+\theta_{(1\times1)}$. These two expressions can now be used to determine the amount of Ag in the $c(2\times2)$ alloy and (1×1) overlayer at $\theta_{I\,max}$, $\theta_{c(2\times2)}=1-\theta_{I\,max}$ and $\theta_{(1\times1)}=2\theta_{I\,max}-1$. Similar to the first scenario, the intensity would then decrease after the intensity peak at $\theta_{I\,max}$ as the $c(2\times2)$ alloy component is covered by Ag. However, unlike the first scenario, the intensity minimum would eventually be reached when the surface is covered by a mixture of (1×1) overlayer and $c(2\times2)_{1.5}$ alloy, expressed as $1=A_{c(2\times2)1.5}+A_{(1\times1)}=(2/3)\theta_{c(2\times2)1.5}+\theta_{(1\times1)}$, and at a coverage of $\theta_{c(2\times2)1.5}+\theta_{(1\times1)}$. Equating the area of the $c(2\times2)_{1.5}$ alloy at that point with the area of the $c(2\times2)$ alloy at $\theta_{I\,max}$, $(2/3)\theta_{c(2\times2)1.5}=2\theta_{c(2\times2)}=2(1-\theta_{I\,max})$, we obtain an expression for the coverage that the intensity reaches a minimum in terms of $\theta_{I\,max}$, $\theta_{c(2\times2)1.5}+\theta_{(1\times1)}=2-\theta_{I\,max}$. This decreases from 1.5 ML toward 1 ML as $\theta_{I\,max}$ increases from 0.5 ML to 1.0 ML at lower deposition temperature [Fig. 5(b)], in qualitative agreement with the experimental observations [Fig. 5(a)]. We will proceed to analyze the data according to the second scenario, since it appears to be more consistent with the theoretical and experimental results than the first scenario. The analysis focuses on the parallel formation of $c(2\times2)$ alloy and (1×1) overlayer up to $\theta_{I\,max}$ and does not concern the formation of the $c(2\times2)_{1.5}$ structure by overgrowth of the $c(2\times2)$ alloy beyond that point.

The parallel formation of (1×1) overlayer and $c(2\times2)$ alloy is modeled by the following rate equations:

$$\frac{d\theta_1}{dt}=R[1-\alpha(2\theta_{c(2\times2)})]-R_{ex}\theta_1(\text{eff}), \qquad (1a)$$

$$\frac{d\theta_{c(2\times2)}}{dt}=R\alpha(2\theta_{c(2\times2)})+R_{ex}\theta_1(\text{eff}), \qquad (1b)$$

where θ_1 is the coverage of Ag atoms in the overlayer, $\theta_{c(2\times2)}$ is the alloy coverage, R is the deposition rate, R_{ex} is the rate that Ag atoms exchange from positions in the overlayer to the alloy sites, and the quantities $\theta_1(\text{eff})$ and α will be explained shortly. Note that θ_1 includes individual adatoms on the pure, unalloyed Mo(100) surface as well as atoms that are present in the (1×1) overlayer phase on the pure Mo(100) surface. The first terms in this pair of equations are related to the deposition of Ag into the overlayer on areas unclaimed by the alloy [Eq. (1a)] and deposition onto the alloy [Eq. (1b)]. A portion, α (where $0\leq\alpha\leq1$), of the atoms that land on the alloy will become incorporated into the alloy when they diffuse to the edge of the alloyed regions. The complementary portion, $(1-\alpha)$, diffuses off of the alloy and into the overlayer. In the extreme case $\alpha=0$ ($\alpha=1$), all (none) of the atoms that land on the alloy are transferred to the overlayer. The second terms of these equations describe the exchange of Ag atoms from overlayer to alloy sites. Here the quantity $\theta_1(\text{eff})$ indicates the coverage of overlayer atoms that can effectively exchange into the alloy [$\theta_1(\text{eff})\leq\theta_1$]. In the application of these rate equations to the analysis of the data, we will examine how the variation of α and $\theta_1(\text{eff})$ affect the outcome.

The aim of the analysis is to determine the rate of exchange, R_{ex}, for each deposition temperature, from which an activation energy can be determined. We begin by integrating the rate equations, Eq. (1), until the total coverage is equal to $\theta_{I\,max}$. Suitable values of R_{ex} are those that produce $\theta_{c(2\times2)}$ and $\theta_{(1\times1)}$ that satisfy the condition on the area fractions, $1=2\theta_{c(2\times2)}+\theta_{(1\times1)}$, at that point. We first consider the case $\theta_1(\text{eff})=\theta_1$. The logarithm of R_{ex} is plotted vs inverse temperature in Fig. 5(c) for the mean deposition rate of 0.29 ML/min and the limiting cases of $\alpha=0$ and $\alpha=1$. The slopes of the best fit lines in this figure correspond to activation energies for exchange of $E_{ex}=0.55\pm0.09$ eV for $\alpha=0$ and $E_{ex}=0.48\pm0.08$ eV for $\alpha=1$.

We now consider the case that $\theta_1(\text{eff})<\theta_1$ due to a "steric" constraint. Steric constraint here simply means that alloy formation is inhibited in the (1×1) areas of the overlayer. To quantify this, we first identify the quantity $\theta_1'=\theta_1/(1-2\theta_{c(2\times2)})$. This is the local overlayer coverage on the area that is unclaimed by the alloy. In a mean-field sense, steric constraint to alloy formation occurs when $0.5<\theta_1'\leq1$, because some portion of the overlayer must be in the (1×1) phase on average in this range. That portion can be straightforwardly shown to be $\theta_{(1\times1)}=(2\theta_1'-1)(1-2\theta_{c(2\times2)})$, while the remaining portion is isolated Ag adatoms and provides the definition of $\theta_1(\text{eff})=(1-\theta_1')(1-2\theta_{c(2\times2)})$. Note that these definitions yield $\theta_{(1\times1)}+\theta_1(\text{eff})=\theta_1$, as they should. When $\theta_1'=1$, they also simplify to $\theta_1(\text{eff})=0$ and $\theta_{(1\times1)}=\theta_1$. This means that all overlayer atoms are in the (1×1) phase at that point, which by definition occurs at $\theta_{I\,max}$. The exchange from overlayer to alloy is also quenched at that point according the second terms in Eq. (1).

On the other hand, steric constraint is absent and $\theta_1(\text{eff})$ $= \theta_1$ when $\theta_1' \leqslant 0.5$. The rate of exchange, R_{ex}, is then determined by integrating the rate equations, as above, using the definition of $\theta_1(\text{eff})$ subject to steric constraint. In this case, the plots of the logarithm of R_{ex} vs inverse temperature have a similar linear appearance as the plots in Fig. 5(c). Activation energies for exchange subject to steric constraint are determined from the slopes of these plots to be E_{ex} $= 0.52 \pm 0.09$ eV for $\alpha = 0$ and $E_{ex} = 0.44 \pm 0.08$ eV for $\alpha = 1$.

Nearly identical activation energies are determined also for the other deposition rates that were used in the experiment. This occurs in the analysis because the optimal fit to the data apparently forces R_{ex} to be proportional to R. The ratio of the formation rates of overlayer and alloy [divide Eq. (1a) by Eq. (1b)] is then independent of R. In this way, the rate equation model can account for the experimental observation that the value of $\theta_{I\,max}$ is independent of deposition rate within experimental uncertainty.

The dependence of $\theta_{I\,max}$ upon deposition temperature can now be predicted using the rate equations. This is shown by the solid curve in Fig. 5(b) for the case of $\theta_1(\text{eff}) = \theta_1$, $\alpha = 1$. This model predicts that the alloy does not form during deposition at 300 K and the weak onset of alloy formation during deposition above about 400 K. Similar results are obtained for the other cases of $\theta_1(\text{eff})$ and α that were considered. This is in agreement with experimental observations of periodic diffraction intensity oscillations that indicate layer-by-layer growth during deposition at 300 K.

D. Diffusion

The maximum $c(2 \times 2)$ integrated intensity during Ag deposition depended strongly on the deposition rate and deposition temperature [Fig. 7(a)]. Specifically, we found that the maximum $c(2 \times 2)$ integrated intensity decreased when the deposition rate was increased in the range from 0.04 to 0.80 ML/min. The $c(2 \times 2)$ integrated intensity also decreased when the deposition temperature was reduced in the range from 792 to 649 K. Similar systematic experiments were not performed at lower temperature. The $c(2 \times 2)$ intensity data shown in Fig. 7(a) were all obtained under identical diffraction conditions, i.e., incident electron energy, $E = 25$ eV, and normal incidence. All of the data for different rates at the same temperature were obtained on the same day in random order. This means that the systematic dependence of intensity upon deposition rate shown in Fig. 7(a) is not caused by other unknown factors. The instrumental parameters that affect the measured intensity (incident beam current, detector signal amplification) were also calibrated on different days by repeating standard deposition temperature and rate conditions ($T = 792$ K, $R = 0.14$ ML/min).

Because of the basic relationship between integrated $c(2 \times 2)$ intensity and $c(2 \times 2)$ coverage, $\theta_{c(2\times2)}$, we must first consider the possibility that the behavior shown in Fig. 7(a) is another manifestation of the exchange kinetic limitation, which is the subject of Sec. III C. However, it was clearly shown [cf. Fig. 5(b)] that the kinetic limitation to alloy formation is minimal at 750 K and above. Although the ex-
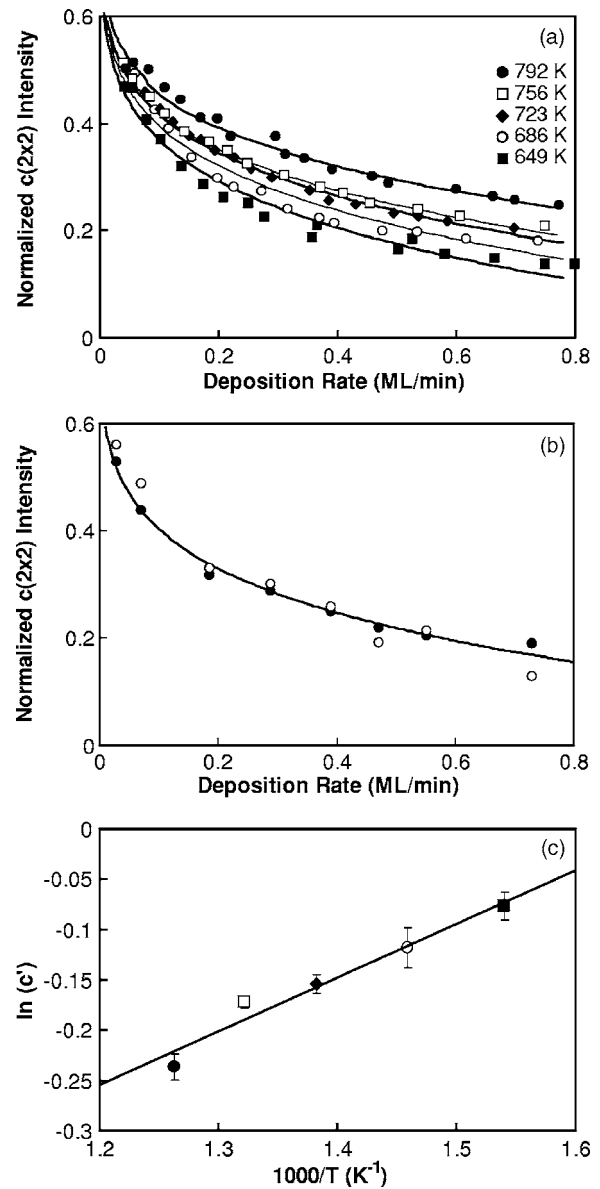

FIG. 7. (a) The dependence of the maximum $c(2 \times 2)$ integrated diffraction intensity at the $(\frac{1}{2}\,\frac{1}{2})$ positions upon deposition rate is shown for several indicated deposition temperatures. The solid curves through the data points are the fit of Eq. (3) with best fit parameters $i = 1$ and c' (c' defined in the text) that are shown in panel (c). (b) The normalized intensity determined from the $c(2 \times 2)$ diffraction linewidth using Eq. (4) ($\bigcirc$) and by integrating the diffraction lineshape ($\bullet$) are plotted vs deposition rate for deposition at 700 K. (c) The logarithm of c' determined from fitting the data in panel (a) is plotted with corresponding symbols vs inverse temperature. The incident electron energy was 25.0 eV.

change kinetic limitation is responsible for reducing the optimum $c(2 \times 2)$ coverage, $\theta_{c(2\times2)} < 0.5$ ML, at lower temperature, it was also noted in Sec. III C that this effect is apparently independent of the deposition rate within experimental uncertainty. We must also point out here that the integrated intensities in Fig. 7(a) have been normalized to unity at deposition rate $R = 0$ through the model described below. This normalization already accounts for the reduction

of the $c(2\times2)$ coverage due to the exchange kinetic limitation at lower temperatures. Even after normalization, the $c(2\times2)$ intensity exhibits a strong temperature dependence in Fig. 7(a) that is about a factor of three times stronger than could be attributed to the kinetic limitation to alloy formation.

We suggest that the behavior depicted in Fig. 7(a) may be a consequence of nucleation processes that occur during alloy formation. There exist two $c(2\times2)$ sublattices on the Mo(100) surface that are laterally shifted by one lattice vector in the surface [010] or [100] directions (Fig. 1). Alloy domains nucleate randomly and with equal probability on the two sublattices. Coalescence of $c(2\times2)$ domains that nucleate on the same sublattice do not disrupt the $c(2\times2)$ structure. However, coalescence of "antiphase" $c(2\times2)$ domains that reside on different sublattices produces a domain wall (Fig. 1). It is also already established (cf. Fig. 4) that nucleation and growth of compact alloy islands occurs during alloy formation. Due to the shifted registry of adjacent layers at the body-centered-cubic (bcc) (100) surface, an effective domain wall is also present at every atomic step between alloy islands and the alloy in the surrounding terrace (Fig. 1). If the domain walls within a terrace or the island edge perimeters scatter weakly into the $c(2\times2)$ diffraction positions, then the integrated diffraction intensity will be sensitive to the total domain wall and/or island edge lengths. This would be the case if the scattered intensity from these boundaries appears away from the $c(2\times2)$ diffraction positions for any reason, for example, if the boundary is disordered and produces a diffuse intensity over the entire Brillouin zone. The total boundary lengths are related to the domain and island densities. Therefore, the dependence of the integrated intensity on the deposition temperature and rate [Fig. 7(a)] is ultimately determined by the details of domain and/or island nucleation kinetics.

To begin with, we write the integrated intensity with weakly scattering domain walls (or island perimeters) present as

$$I = I_o\left(1 - c_o\frac{\delta N}{N}\right), \tag{2}$$

where I_o is the intensity for a perfect single domain surface alloy with no walls, N is the total number of Ag atoms embedded in the alloy and illuminated by the incident beam, δN is the number of those atoms that reside in domain walls, and c_o describes the suppression of scattering into the $c(2\times2)$ positions by domain walls ($0 \leq c_o \leq 1$). The number δN is proportional to the domain wall length (and width). Domain walls form in the alloy when all of the nucleated (antiphase) domains coalesce. Therefore, the total domain wall length is proportional to the perimeter of all domains. Assuming that n compact domains nucleate, the total domain wall length scales as $\sim n^{1/2}$.[39] Therefore, the key to understanding the experimental data in Fig. 7(a) lies in appreciating how the saturation domain number depends upon deposition temperature and rate. Similar statements can be made for weakly scattering alloy island perimeters, except that alloy islands do not coalesce [see Fig. 4(e)].

According to the classical theory for overlayer island nucleation, the saturation island number for the case of complete condensation in two dimensions is given by $n \sim R^{i/(i+2)}e^{(E_i+iE_{dif})/(i+2)kT}$, where i is the critical island size, E_i is the critical island binding energy, and E_{dif} is the diffusion energy.[40] We propose that this result also applies to two-dimensional surface alloy domain nucleation. Substituting the nucleation theory result for the saturation number into the expression for the intensity [Eq. (2)], we obtain

$$I \sim I_o(1 - cR^{i/2(i+2)}e^{(E_i+iE_{dif})/2(i+2)kT}), \tag{3}$$

where c is the product of c_o and proportionality constants relating $\delta N/N$ to $n^{1/2}$ and n to R.

The expression for the intensity, Eq. (3), was fit to the rate-dependent integrated $c(2\times2)$ intensity data for each temperature, treating $c'=ce^{(E_i+iE_{dif})/2(i+2)kT}$ and i as fit parameters, with encouraging results that are indicated by the solid curves through the data points in Fig. 7(a). The best fit value of $i=1$ and the values of c' that are shown in Fig. 7(c) were determined for the different temperatures. For the case of $i=1$, the binding energy is $E_i=0$ by definition.[41] Therefore, the slope of $\ln(c')$ vs inverse temperature in Fig. 7(c) determines the diffusion energy $E_{dif}=0.25\pm0.03$ eV.

The assessment of nucleation kinetics based on treatment of the integrated $c(2\times2)$ diffraction intensity is verified by examining the $c(2\times2)$ diffraction line shape, which provides an independent and direct measure of feature size. In particular, the characteristic feature size (domain or island radius) is given by $r=2\pi/\Gamma$, where Γ is the $c(2\times2)$ diffraction spot full width at half maximum (FWHM) after deconvolution of the instrumentally limited width. The instrumentally limited diffraction spot had a Gaussian line shape with a FWHM of 0.03 Å^{-1}, corresponding to an instrumental transfer width of just over 400 Å. According to the arguments given above, the saturation domain or island number n increases when the deposition temperature is reduced or when the deposition rate is increased. The feature size must also decrease in a way that is consistent with the increase of the feature number. For compact domains or islands, the perimeter of a single feature, P_1, is proportional to r and the feature area, A_1, is proportional to r^2. Equation (2) can now be written in a form related to the quantities P_1 and A_1 as

$$I = I_o\left(1 - c''\frac{P_1}{A_1}\right), \tag{4}$$

where c'' contains information about the width of the weakly scattering boundary (domain wall or island edge) and its possible lengthening due to meandering about the mean compact feature shape. In other words, c'' is an effective width. For circular or square features, $P_1/A_1=2/r$. From analysis of the $c(2\times2)$ diffraction spot profile, we find that r decreases from 91 Å to 46 Å when the deposition rate is increased from 0.03 ML/min to 0.73 ML/min at 700 K. The corresponding variation of the normalized $c(2\times2)$ intensity, I/I_o, according to Eq. (4) is shown in Fig. 7(b). For comparison, Fig. 7(b) also shows the normalized integrated intensity, which is obtained simultaneously by integrating the lineshape, and the best fit of Eq. (3) with $i=1$ and $\ln(c')$

=−0.131. This value of ln(*c*′) is consistent with the others in Fig. 7(c). A value of *c*″=10 Å has been used to scale the result of the lineshape FWHM analysis, Eq. (4), to the integrated intensity results, Eq. (3), in Fig. 7(b). The strong similarity of the results obtained by two approaches confirms that nucleation kinetics are responsible for the observed deposition rate and temperature dependence of the integrated c(2×2) diffraction intensity during alloy formation.

E. Desorption

The alloy order-disorder transition that is indicated by the sharp decrease of the c(2×2) integrated diffraction intensity above 800 K (Fig. 6) is obviously one factor that sets an upper temperature limit on the existence of the alloy. Additionally, evidence of desorption was observed at temperatures exceeding 990 K, i.e., near the inflection point of the disordering transition. Desorption was evident in the response of the c(2×2) intensity under different conditions. First, in order to maintain a constant c(2×2) intensity over time in this temperature range, it was necessary to establish adsorption/desorption balance by exposing the surface continuously to an incident Ag flux from the deposition source. Excessive or insufficient deposition flux caused the c(2×2) intensity to decrease due to Ag coverage exceeding or falling short of the ideal, 0.5 ML, respectively. At higher temperatures, exposure to a higher incident flux was required in order to establish the adsorption/desorption balance and to maintain a constant c(2×2) intensity. Alternatively, the surface could be cycled through the ideal coverage by repeatedly depositing slightly in excess and desorbing to slightly less than 0.5 ML coverage. During this procedure, the c(2×2) intensity repeatedly increased and decreased, attaining a maximum each time the coverage passed through 0.5 ML during adsorption and desorption [Fig. 8(a)]. We take advantage of this effect to determine the desorption energy.

The desorption energy was determined as follows. At fixed temperature, Ag was deposited to a coverage slightly, $d\theta$ ML, in excess of the ideal coverage of 0.5 ML. Then, the time required, dt, to desorb the excess material in the absence of the incident Ag flux was determined by monitoring the rise of the c(2×2) intensity to a peak.[42] For example, Fig. 8(a) shows the rise of the c(2×2) intensity during desorption of excess Ag at 995 K. Assuming first-order desorption kinetics, the desorption rate is equal to the Ag coverage times the usual Arrhenius expression for the desorption rate

$$\frac{d\theta}{dt} = \theta(\nu e^{-E_{des}/kT}), \qquad (5)$$

where E_{des} is the desorption energy and ν is the attempt frequency. The complication is that the surface is not homogeneous at these temperatures. Part of the Ag is in alloy sites and part is in overlayer sites. A further complication is that the inhomogeneity varies as the temperature is changed (see Fig. 6). Desorption may take place uniformly from all sites, from c(2×2) alloy only or from the disordered overlayer only. Fortunately, the portion of Ag in alloy sites is known from the normalized c(2×2) intensity, I_{norm}, shown in Fig. 6.

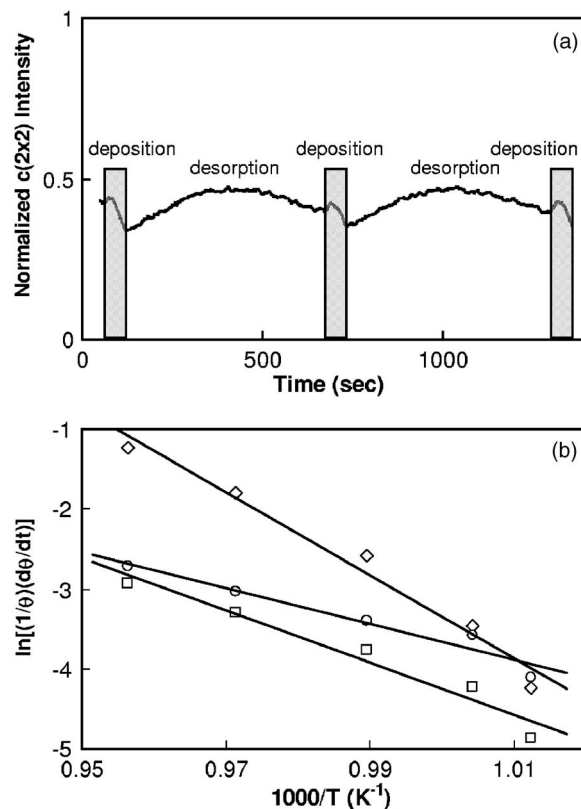

FIG. 8. (a) The c(2×2) integrated intensity passes through a maximum while the Ag coverage is cycled repeatedly through the ideal coverage, 0.5 ML, during deposition and desorption intervals at constant temperature, 995 K. The amount of Ag deposited in each 1 min deposition interval is 0.08 ML. The incident electron energy was 25.0 eV. (b) A plot of the logarithm of the desorption rate weighted by the coverage [see Eq. (5)] vs inverse temperature exhibits linear behavior for three cases considered, (□) desorption from alloy and disordered overlayer sites simultaneously, (◇) from alloy sites only, (○) and from disordered overlayer sites only.

The normalized intensity of 1 below 800 K corresponds to 100% of the Ag, or 0.5 ML, in alloy sites. The Ag coverage in alloy sites above 800 K is then just $\theta_{c(2\times2)}=(0.5$ ML)I_{norm}. The amount of Ag in disordered overlayer sites is complementary, $\theta_{over}=(0.5$ ML)$(1-I_{norm})$. The desorption energy is then determined by examining a plot of $\ln[(1/\theta)(d\theta/dt)]$ vs inverse temperature. This is shown in Fig. 8(b) for the three possible choices of $\theta=0.5$ ML, $\theta_{c(2\times2)}$, and θ_{over}. Approximate linear behavior is observed with slopes that correspond to desorption activation energies of E_{des} =2.81±0.34 eV, 4.48±0.41 eV, and 1.94±0.26 eV for desorption from alloy and overlayer simultaneously, alloy only, and overlayer only, respectively. The corresponding desorption prefactors that are determined from the intercepts of the lines in Fig. 8(b) at 1000/T=0 are ν=2.0×10$^{12\pm1.7}$ s^{-1} (alloy and overlayer simultaneously), 1.9×10$^{20\pm2}$ s^{-1} (alloy only), and 1.6×10$^{8\pm1.3}$ s^{-1} (overlayer only).

IV. DISCUSSION

The dependence of the integrated c(2×2) diffraction intensity upon deposition rate and temperature reveals how

elementary kinetic processes—exchange, nucleation, diffusion, and desorption—can affect the formation and ordering of the Ag-induced $c(2\times2)$ alloy at the Mo(100) surface. A kinetic limitation to alloy formation, which is believed to be imposed by an activation barrier for exchange of Ag for surface Mo atoms, becomes evident during deposition below about 750 K. A signature of this kinetic limitation is that the optimal formation of the $c(2\times2)$ alloy is delayed until a Ag coverage is reached that exceeds the ideal coverage, 0.5 ML, of the alloy. The required excess increases as the deposition temperature is lowered [Fig. 5(a)]. The view that we have taken is that the excess material is consumed by the formation of a (1×1) Ag overlayer in parallel with the alloy and/or by the overgrowth of the alloy by a Ag layer prior to the optimal Ag coverage. The overgrown alloy is also referred to as a $c(2\times2)_{1.5}$ alloy. Theoretical calculations (Fig. 2) indicate that both the (1×1) overlayer and the $c(2\times2)_{1.5}$ alloy are metastable at coverages of less than 0.5 ML. However, the (1×1) overlayer is the energetically favored of these two metastable structures. The implication is that Ag may migrate off of the $c(2\times2)$ alloy and onto the pure Mo surface, but the reverse will not happen. Additional detailed arguments have been given in Sec. III C as to why the overgrowth of the alloy is an unlikely cause for the required Ag excess.

An activation barrier for alloy formation is determined from the temperature dependence of the required Ag excess using a mean-field rate equation model [Eq. (1)]. Various cases were considered by setting parameters, α and $\theta_1(\text{eff})$, in the model. The parameter α ($0\le\alpha\le1$) describes the fate of Ag atoms that are deposited directly on the alloy. In one extreme case, $\alpha=0$, all atoms that are deposited on the alloy migrate to areas that are unclaimed by the alloy and add to the coverage, θ_1, on these areas. In the other extreme, $\alpha=1$, atoms that are deposited on the alloy eventually incorporate into the alloy without first adding to θ_1. Activation energies of $E_{ex}=0.55\pm0.09$ eV for $\alpha=0$ and $E_{ex}=0.48\pm0.08$ eV for $\alpha=1$ are determined when all of the atoms present on areas unclaimed by alloy can effectively exchange, $\theta_1(\text{eff})=\theta_1$. On the other hand, activation energies of $E_{ex}=0.52\pm0.09$ eV for $\alpha=0$ and $E_{ex}=0.44\pm0.08$ eV for $\alpha=1$ are determined when we consider that some portion of θ_1 must reside in the (1×1) overlayer on average, and this portion is excluded from exchanging into the alloy. This case is described in more detail in Sec. III C. The average of the activation energies for these four cases, $E_{ex}=0.50\pm0.17$ eV, is taken to be the characteristic barrier. We also note that the linear fits to the data in Fig. 5(c) imply characteristic attempt frequencies that are orders of magnitude smaller than the typical frequency, 10^{12}–10^{13} s^{-1}, for atomic processes. This highlights the shortcoming of a rate equation model, which contains no information on the spatial dependence of the exchange process. For example, exchange may occur at the edges of existing alloy domains, at steps, or through the concerted effort of two or more Ag atoms. In other words, it is difficult to interpret the attempt frequency that is determined by the rate equation model. Despite this shortcoming, the rate equation model and the obtained parameters correctly predict that the alloy does not form during deposition at 300 K [solid line in Fig. 5(b)], in agreement with experimental observations.

A well-ordered Pd-induced $c(2\times2)$ alloy was also produced on the Mo(100) surface if deposition was carried out at 780 K, but the formation of this alloy was noticeably suppressed during deposition at 580 K.[25] Similarly, annealing at 800 K was required to produce $c(2\times2)$ alloys on the W(100) surface from metal overlayers that were deposited at 300 K.[22–24] For comparison, several $c(2\times2)$ alloys are known to form on fcc (100) surfaces without any apparent exchange limitation at 300 K or below, in some cases, including alloys of Au,[4] Pd,[5] Mn,[6] and Mg[7] on Cu(100), Mn[8] and Sn[9] on Ni(100), Mn on Pd(100),[10] Ag(100),[11] and Co/Cu(100),[12] Li[13] on Al(100), and Au[14] on Mn(100). A Sn-induced $p(3\sqrt{2}\times\sqrt{2})R45°$ alloy, which is closely related to the $c(2\times2)$ alloy structure, also forms on the Cu(100) surface at 300 K.[15] Similar to the $c(2\times2)$ alloys on Mo(100) and W(100), these alloys are confined to the topmost layer and contain 0.5 ML of deposited metal atoms. The formation of these fcc (100) surface alloys at low temperature implies that the exchange barriers on the fcc (100) surfaces are smaller than on W(100) and Mo(100). Besides different substrate crystal structures, this particular difference between the alloy formation kinetics on bcc Mo(100), W(100), and the fcc metal (100) surfaces is consistent with differences in the substrate bulk cohesive energies, which are 6.82 eV/atom for Mo and 8.90 eV/atom for W as compared to 2.92 (Mn), 2.95 (Ag), 3.39 (Al), 3.49 (Cu), 3.89 (Pd), and 4.44 (Ni) eV/atom.[36] The corresponding quantity for fcc Co films on Cu(100) probably does not exceed the value of 3.49 eV/atom for bulk Co. On the other hand, the formation of some other $c(2\times2)$ alloys at the fcc(100) surfaces are known to require thermal activation above 300 K, including Pt/Cu(100),[16,17] Al/Ni(100),[18] and Mn/Au(100).[19] However, there is good evidence that deposited metal atoms penetrate beyond the surface layer in these alloys. A transition from surface layer to subsurface layer sites also occurs upon annealing the Cu(100)-Pd $c(2\times2)$[20] and Pd(100)-Mn $c(2\times2)$[10,21] alloy systems. Penetration of metal atoms beyond the surface layer involves a more dramatic atomic rearrangement and therefore confronts a larger activation barrier.

We have also found striking evidence that disorder is introduced during alloy formation and that the degree of disorder is dictated by nucleation kinetics. This evidence is present in the dependence of the $c(2\times2)$ integrated diffraction intensity and diffraction linewidth upon deposition temperature and deposition rate (Fig. 7). The perimeters of alloy islands and antiphase domain walls that form when antiphase alloy domains converge are identified as two possible locations of alloy disorder. A general model, which employs an expression for the saturation island number from classical nucleation theory to describe nucleation kinetics of either feature (islands or domains), can account for the experimental results. Further investigations are required to distinguish whether domain walls or island edges or both are responsible for modifying the diffraction intensity and diffraction linewidth. Nevertheless, the present lack of clarity on this point does not affect the conclusion that nucleation kinetics influence the alloy formation and ordering, or the reliability of the critical feature (island or domain) size and diffusion energy
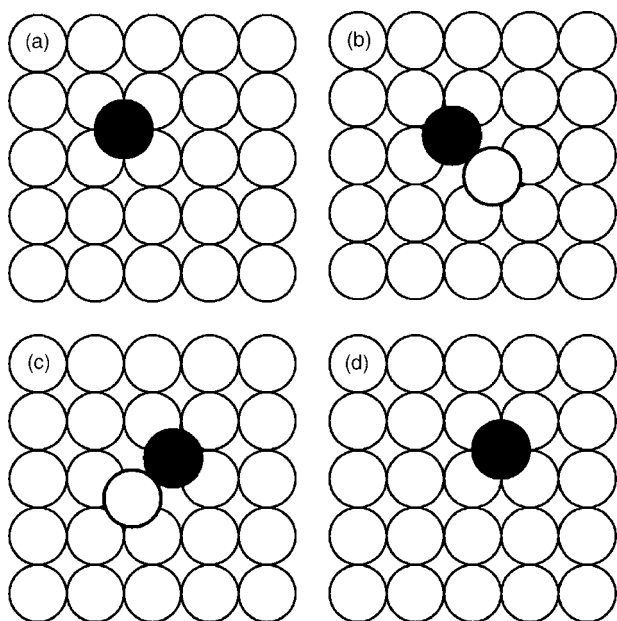
FIG. 9. Diffusion mediated by a Ag-Mo-vacancy complex involves (a) a Ag adatom (shaded circle) on the Mo (unshaded circles) surface, (b) formation of a vacancy complex, (c) in-plane rotation of the vacancy complex by 90°, and (d) unbinding of the vacancy complex which produces a Ag adatom that is displaced by one lattice site from (a).

that are determined by the analysis. This analysis reveals that the critical feature size is $i=1$, a result that is often found in island nucleation on (100) surfaces.[41] The diffusion energy that was determined from this analysis, $E_{dif}=0.25\pm0.03$ eV, is somewhat smaller than diffusion energies that are typically found for hopping diffusion on open metal surfaces, such as the bcc(100).[43] For example, the activation energy for Ni diffusion on the W(100) surface was determined to be $E_{dif}=1.03$ eV.[44]

The low diffusion barrier that is determined here is reminiscent of the low barriers that may be associated with an exchange diffusion mechanism. For example, first principles theoretical calculations showed that the barrier for self diffusion by an exchange mechanism is a factor of three lower than the hopping diffusion barrier on the Al(100) surface.[45] The fault with this explanation for Ag diffusion on Mo(100) is that an exchange produces a Mo adatom and immobilizes the Ag atom. Instead, we suggest that diffusion is mediated by the formation and motion of an intermediate Ag-Mo-vacancy complex prior to exchange (Fig. 9). This complex is modeled on the precedent Re-Ir-vacancy complex that was observed on the Ir(100) surface with field ion microscopy.[46] The Re-Ir-vacancy complex is produced by partial displacement of the substrate Ir atom out of the surface and partial insertion of the Re atom along the in-plane surface [110] or equivalent directions [Fig. 9(b)]. It was also observed that the Re-Ir-vacancy complex can rotate in-plane by 90° [Fig. 9(c)]. This is crucial if the vacancy complex is to mediate diffusion of Ag on the Mo(100) surface. In particular, we propose that the Ag-Mo-vacancy complex can also unbind after rotation, thereby producing a Ag adatom that is displaced from its initial position by one lattice site in the surface [100] direction [Fig. 9(d)]. The Ag adatom is then free to form another Ag-Mo-vacancy complex with any of the four underlying Mo atoms. Repeated vacancy complex formation, rotation, and unbinding can accomplish diffusive motion over large distances. The physical picture that emerges from these investigations is that Ag adatoms diffuse on the Mo(100) surface by the formation and motion of Ag-Mo-vacancy complexes with a low activation barrier. Unbinding of the Ag-Mo-vacancy complex that results in a Ag atom embedded in the surface occurs less frequently due to the somewhat higher exchange barrier.

Finally, we remark on the thermal desorption of Ag at elevated temperature. Desorption ultimately prevents condensation of sufficient material to attain the ideal $c(2\times2)$ coverage of 0.5 ML, unless the deposition rate is increased appropriately. However, compensation of desorption flux by increasing the deposition flux at higher temperature does have its limits. Evidence of thermal desorption was observed at temperatures above the inflection point of an order-disorder phase transition of the alloy. The transition converts the ordered alloy to a disordered overlayer. Therefore, three possible situations were considered in the analysis of the desorption energy. These were that desorption takes place from alloy sites only, from disordered overlayer sites only, or effectively from both overlayer and alloy sites, and the corresponding results for the desorption energy for these three possibilities were $E_{des}=4.48\pm0.41$ eV, 1.94 ± 0.26 eV, and 2.81 ± 0.34 eV, respectively. Assuming detailed balance, we believe that desorption must be treated in the analysis as deriving from both alloy and overlayer sites simultaneously. In support of this conclusion, we note that the desorption prefactor that was determined for this case, $\nu=2.0\times10^{12\pm1.7}$ s^{-1}, is physically reasonable. The desorption prefactors that were determined assuming that desorption occurred from overlayer sites only or from alloy sites only were orders of magnitude smaller or larger, respectively, which are unphysical. These two possibilities must therefore be ruled out.

V. CONCLUSIONS

The formation of the Mo(100)-Ag $c(2\times2)$ surface alloy is influenced by the kinetics of several atomistic processes. Disorder is built into the alloy during the formation process to a degree that is determined by nucleation kinetics, which are governed by diffusion. Disorder may be related either to domain walls that form upon coalescence of antiphase domains or to alloy island perimeters. An expression for the saturation island number from classical nucleation theory is a central part of a model that is introduced to evaluate the data, and that is generally applicable to either source of disorder. A diffusion energy is determined from the analysis, $E_{dif}=0.25\pm0.03$ eV. This is unusually low for hopping diffusion on an open bcc (100) surface and is attributed instead to a partial exchange diffusion mechanism mediated by a Ag-Mo-vacancy complex. Further work is needed to clarify the dominant source of alloy disorder. If domain walls are responsible, then we can conclude that domain nucleation is governed by atomistic processes that are analogous to those

that dictate overlayer island nucleation. A kinetic limitation to alloy formation, which is believed to be associated with the exchange of Ag for Mo surface atoms, is also observed during Ag deposition below 750 K. A rate equation model is presented that includes the formation of a Ag overlayer and $c(2\times2)$ alloy in parallel and in series. The controlling activation barrier is determined from the model analysis to be E_{ex}=0.50±0.17 eV. This model also correctly predicts that the alloy does not form at 300 K, in agreement with experimental observations. Thermal desorption of Ag is also observed at above 950 K, which prevents condensation of suf-

ficient material to attain the ideal $c(2\times2)$ coverage of 0.5 ML unless the deposition rate is increased appropriately. The desorption energy E_{des}=2.81±0.34 eV and prefactor ν=2.0 $\times10^{12\pm1.7}$ s^{-1} were determined.

*Corresponding author. Electronic address: phaltman@ust.hk

[1] U. Bardi, Rep. Prog. Phys. **57**, 939 (1994).

[2] J. A. Rodriquez, Surf. Sci. Rep. **24**, 223 (1996).

[3] *Alloy Surfaces and Surface Alloys*, edited by D. P. Woodruff, The Chemical Physics of Solid Surfaces, Vol. 10 (Elsevier, Amsterdam, 2002).

[4] Z. Q. Wang, Y. S. Li, C. K. C. Lok, J. Quinn, F. Jona, and P. M. Marcus, Solid State Commun. **62**, 181 (1987).

[5] S. H. Lu, Z. Q. Wang, S. C. Wu, C. K. C. Lok, J. Quinn, Y. S. Li, D. Tian, F. Jona, and P. M. Marcus, Phys. Rev. B **37**, 4296 (1988).

[6] M. Wuttig, Y. Gauthier, and S. Blügel, Phys. Rev. Lett. **70**, 3619 (1993).

[7] M. S. Chen, D. Terasaki, S. Mizuno, H. Tochihara, I. Ohsaki, and T. Oguchi, Surf. Sci. **470**, 53 (2000).

[8] M. Wuttig, C. C. Knight, T. Flores, and Y. Gauthier, Surf. Sci. **292**, 189 (1993).

[9] Y. D. Li, L. Q. Jiang, and B. E. Koel, Phys. Rev. B **49**, 2813 (1994).

[10] D. Tian, R. F. Lin, F. Jona, and P. M. Marcus, Solid State Commun. **74**, 1017 (1990).

[11] P. Schieffer, C. Krembel, M. C. Hanf, and G. Gewinner, Phys. Rev. B **55**, 13884 (1997).

[12] B.-Ch. Choi, P. J. Bode, and J. A. C. Bland, Phys. Rev. B **58**, 5166 (1998).

[13] J. H. Petersen, A. Mikkelsen, M. M. Nielsen, and D. L. Adams, Phys. Rev. B **60**, 5963 (1999).

[14] T. K. Yamada, A. L. Vázquez de Parga, M. M. J. Bischoff, T. Mizoguchi, and H. van Kempen, Surf. Sci. **600**, 1048 (2006).

[15] K. Pussi, E. AlShamaileh, E. McLoughlin, A. A. Cafolla, and M. Lindroos, Surf. Sci. **549**, 24 (2004).

[16] G. W. Graham, P. J. Schmitz, and P. A. Thiel, Phys. Rev. B **41**, 3353 (1990).

[17] E. Al Shamaileh, C. J. Barnes, and A. Wander, J. Phys. Condens. Matter **15**, 1879 (2003).

[18] S. H. Lu, D. Tain, Z. Q. Wang, Y. S. Li, F. Jona, and P. M. Marcus, Solid State Commun. **67**, 325 (1988).

[19] W. Kim, S.-J. Oh, J. Seo, H. G. Min, S. C. Hong, and J.-S. Kim, Phys. Rev. B **65**, 205407 (2002).

[20] C. J. Barnes, E. Al Shamaileh, T. Pitkänen, P. Kaukasoina, and M. Lindroos, Surf. Sci. **492**, 55 (2001).

[21] A. J. Jaworowski, S. M. Gray, M. Evans, R. Ásmundsson, P. Uvdal, and A. Sandell, Phys. Rev. B **63**, 125401 (2001).

[22] G. A. Attard and D. A. King, Surf. Sci. **188**, 589 (1987).

[23] G. A. Attard and D. A. King, Surf. Sci. **222**, 360 (1989).

[24] P. H. Bu, A. Wander, L. Morales, M. P. Bessent, and D. A. King, Surf. Sci. **286**, L542 (1993).

[25] D. Wu, W. K. Lau, Z. Q. He, Y. J. Feng, M. S. Altman, and C. T. Chan, Phys. Rev. B **62**, 8366 (2000).

[26] K. L. Man, Y. J. Feng, C. T. Chan, and M. S. Altman (unpublished).

[27] F. Soria and H. Poppa, J. Vac. Sci. Technol. **17**, 449 (1980).

[28] J. R. Cerda, F. Soria, F. J. Palomares, and P. L. de Andres, Surf. Sci. **269/270**, 713 (1992).

[29] D. Singh and H. Krakauer, Surf. Sci. **216**, 303 (1989).

[30] J. G. Che, Z. Z. Zhu, and C. T. Chan, Phys. Rev. Lett. **82**, 3292 (1999).

[31] A. J. Melmed, R. T. Tung, W. R. Graham, and G. D. W. Smith, Phys. Rev. Lett. **43**, 1521 (1979).

[32] X. K. Shu, P. Jiang, and J. G. Che, Surf. Sci. **545**, 199 (2003).

[33] D. Vanderbilt, Phys. Rev. B **41**, 7892 (1990); G. Kresse and J. Hafner, *ibid.* **47**, R558 (1993); G. Kresse and J. Furthmüller, *ibid.* **54**, 11169 (1996).

[34] J. P. Perdew, J. A. Chevary, S. H. Vosko, K. A. Jackson, M. R. Pederson, D. J. Singh, and C. Fiolhais, Phys. Rev. B **46**, 6671 (1992).

[35] H. J. Monkhorst and J. D. Pack, Phys. Rev. B **13**, 5188 (1976).

[36] C. Kittel, *Introduction to Solid State Physics* (Wiley, New York, 1976), p. 74.

[37] E. Bauer, Rep. Prog. Phys. **57**, 895 (1994).

[38] T. Matsumoto and A. Ono, Meas. Sci. Technol. **12**, 2095 (2001).

[39] The area per domain is $A_1=A/n$, where A is the total area and n is the number of domains. The perimeter of each compact domain is proportional to the square root of its area, $P_1\sim A_1^{1/2}$. The total perimeter is proportional to the product of the number of domains and the perimeter per domain, $P\sim nA_1^{1/2}\sim n^{1/2}$.

[40] J. A. Venables, Phys. Rev. B **36**, 4153 (1987).

[41] J. A. Venables, *Introduction to Surface and Thin Film Processes* (Cambridge University Press, Cambridge, England, 2000).

[42] The time interval dt actually also includes the short time that the excess Ag is deposited, because desorption continues to take place during the deposition.

[43] G. L. Kellogg, Surf. Sci. Rep. **21**, 1 (1994).

[44] G. L. Kellogg, Surf. Sci. **192**, L879 (1987).

[45] P. J. Feibelman, Phys. Rev. Lett. **65**, 729 (1990).

[46] Tien T. Tsong and C.-L. Chen, Nature (London) **355**, 328 (1992).